Celest Mech Dyn Astr (2009) 103:227–249
DOI 10.1007/s10569-008-9180-3

ORIGINAL ARTICLE

Lagrangian coherent structures in the planar elliptic restricted three-body problem

Evan S. Gawlik · Jerrold E. Marsden · Philip C. Du Toit · Stefano Campagnola

Received: 14 May 2008 / Revised: 22 October 2008 / Accepted: 15 December 2008 /
Published online: 30 January 2009

Abstract This study investigates Lagrangian coherent structures (LCS) in the planar elliptic restricted three-body problem (ER3BP), a generalization of the circular restricted three-body problem (CR3BP) that asks for the motion of a test particle in the presence of two elliptically orbiting point masses. Previous studies demonstrate that an understanding of transport phenomena in the CR3BP, an autonomous dynamical system (when viewed in a rotating frame), can be obtained through analysis of the stable and unstable manifolds of certain periodic solutions to the CR3BP equations of motion. These invariant manifolds form cylindrical tubes within surfaces of constant energy that act as separatrices between orbits with qualitatively different behaviors. The computation of LCS, a technique typically applied to fluid flows to identify transport barriers in the domains of time-dependent velocity fields, provides a convenient means of determining the time-dependent analogues of these invariant manifolds for the ER3BP, whose equations of motion contain an explicit dependency on the independent variable. As a direct application, this study uncovers the contribution of the planet Mercury to the Interplanetary Transport Network, a network of tubes through the solar system that can be exploited for the construction of low-fuel spacecraft mission trajectories.

Electronic supplementary material The online version of this article (doi:10.1007/s10569-008-9180-3) contains supplementary material, which is available to authorized users.

E. S. Gawlik (✉) · J. E. Marsden · P. C. Du Toit
Control and Dynamical Systems, California Institute of Technology 107-81, Pasadena, CA 91125, USA
e-mail: egawlik@caltech.edu

J. E. Marsden
e-mail: marsden@cds.caltech.edu

P. C. Du Toit
e-mail: pdutoit@cds.caltech.edu

S. Campagnola
Aerospace and Mechanical Engineering, University of Southern California, 854 Downey Way,
Los Angeles, CA 90089-1191, USA
e-mail: scampagn@usc.edu

Keywords Three-body problem · Invariant manifolds · Separatrices · BepiColombo mission

1 Introduction

The three-body problem is a dynamical system rich in mathematical intricacy and practical applicability. A classic problem in the study of celestial mechanics, the general three-body problem asks for the motion of three masses in space under mutual gravitational interaction. The benefit to investigating the three-body problem is twofold: results of such studies often bear broader implications in the theory of dynamical systems, and the investigations themselves are patently well-suited to address challenges in Astronomy. In particular, obtaining a global picture of the dynamical barriers that govern the transport of material through a celestial system is an issue of import to scientists in a surprisingly wide range of fields (Dellnitz et al. 2005; Porter and Cvitanović 2005). The main goal of this paper is to use the theory of Lagrangian coherent structures (LCS) introduced by Haller (2001) to determine transport barriers in the elliptic restricted three-body problem (ER3BP).

Koon et al. (2000a) demonstrate that an understanding of transport phenomena in the circular restricted three-body problem (CR3BP), a problem that asks for the motion of a test particle in the presence of two circularly orbiting point masses, can be obtained through investigation of the stable and unstable manifolds of certain periodic solutions to the three-body problem equations of motion. Evidently, a globalization of the stable and unstable manifolds of periodic orbits about the L_1 and L_2 Lagrange points (unstable equilibrium points in the CR3BP) reveals a web of tubes through phase space that form separatrices between its dynamically different regions. This labyrinth of tubes, dubbed an "Interplanetary Transport Network" (Marsden and Ross 2005), can be exploited in a variety of ways, including the explanation of unusual comet trajectories (Koon et al. 2001), the investigation of transport of material throughout the solar system (Gómez et al. 2004), and the construction of orbits with prescribed itineraries for low-fuel spacecraft mission trajectories (Koon et al. 2000c).

Elaborating on the latter notion, the complexities of multi-body dynamics recently have begun to play a more prominent role in the realm of space mission design (Marsden and Ross 2005). Substantial improvements in fuel efficiency for certain classes of missions can be achieved through an exploitation of the natural dynamics of the three-body problem (Koon et al. 2000c). NASA's Genesis Discovery mission, for instance, exploited subtleties in the dynamics of the Sun–Earth–spacecraft three-body system to traverse a route whose intricacies simpler models like the patched conic approximation fail to describe adequately (Koon et al. 1999).

Computational methods for determining the invariant manifolds of dynamical systems are well-developed for autonomous systems of differential equations like those describing the CR3BP (Parker and Chua 1989). When we turn our attention to non-autonomous differential equations, the methods available for computing stable and unstable manifolds are no longer applicable, as the notions of stable and unstable manifolds for time-dependent vector fields are not even well-defined. Such is the case in the elliptic restricted three-body problem, where no choice of reference frame can rid the differential equations of motion of their time dependency. However, (Shadden et al. 2005) shed light on this issue in their development of the theory of LCS for time-dependent flows. In their report, the authors provide a rigorous justification that LCSs–transport barriers in the domains of time-dependent velocity fields that can be computed algorithmically–"represent nearly invariant manifolds even in systems with arbitrary time dependence" under suitable conditions (Shadden et al. 2005).

This report consists of two parts. Section 2 compares two methods of LCS computation applied to the circular restricted three-body problem. The method deemed superior is used in Sect. 3 to compute LCS in three different elliptic restricted three-body systems: a system described by fabricated mass and orbital eccentricity parameters, the Earth–Moon–spacecraft system, and the Sun–Mercury–spacecraft system.

For simplicity and ease of computation, we focus primarily on the *planar* restricted three-body problem in this report, making only brief use of the spatial case out of necessity in connection with the BepiColombo mission, discussed in Sect. 3.4. Unless otherwise specified, references to the circular and elliptic restricted three-body problems in this report are implicitly references to the *planar* CR3BP and the *planar* ER3BP.

1.1 The circular and elliptic restricted three-body problems

This section studies the *planar restricted three-body problem*, starting with the case where the two primaries are in circular orbit and then the case where the primaries are in elliptical orbit about their center of mass.

1.1.1 The circular restricted three-body problem (CR3BP)

The circular restricted three-body problem (CR3BP) considers the motion of a test mass $m_3 = 0$ in the presence of the gravitational field of two primary masses $m_1 = 1 - \mu$ and $m_2 = \mu$ in circular orbit about their center of mass. Throughout this paper, the test particle is assumed to begin in the orbital plane of the two primary masses with its velocity component normal to that plane equal to zero, so that its motion is constrained to the $m_1 - m_2$ orbital plane for all time. Without loss of generality, all units are normalized and positions are defined relative to a rotating coordinate frame whose x-axis coincides with the line joining m_1 and m_2 and whose origin coincides with the center of mass of m_1 and m_2, as shown in Fig. 1. The equations of motion for the test particle are then (Szebehely 1967)

$$\ddot{x} - 2\dot{y} = \frac{\partial \Omega}{\partial x} \tag{1}$$

$$\ddot{y} + 2\dot{x} = \frac{\partial \Omega}{\partial y}, \tag{2}$$

where

$$\Omega(x, y) = \frac{x^2 + y^2}{2} + \frac{1 - \mu}{\sqrt{(x + \mu)^2 + y^2}} + \frac{\mu}{\sqrt{(x - 1 + \mu)^2 + y^2}} + \frac{1}{2}\mu(1 - \mu) \tag{3}$$

and (x, y) denotes the position of m_3 in the rotating frame.

There are five equilibrium points (Lagrange points) L_i, $i = 1, 2, 3, 4, 5$, in the CR3BP (Szebehely 1967), corresponding to critical points of the effective potential Ω. Three of these points (L_1, L_2, and L_3) are collinear with the masses m_1 and m_2, while the remaining two (L_4 and L_5) lie at the vertices of the pair of equilateral triangles whose bases coincide with the line segment joining m_1 and m_2 (see Fig. 2b). Let L_i^x and L_i^y denote the x and y coordinates, respectively, of ith Lagrange point.

It is straightforward to check through differentiation that

$$E(x, y, \dot{x}, \dot{y}) = \frac{1}{2}(\dot{x}^2 + \dot{y}^2) - \Omega(x, y) \tag{4}$$

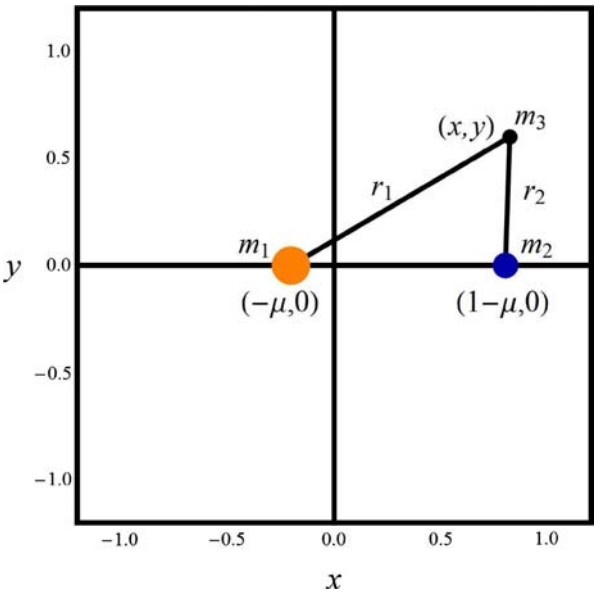

Fig. 1 Rotating coordinate system in the circular restricted three-body problem. All units are nondimensionalized. The coordinate frame rotates counterclockwise with unit angular frequency. In the case of the elliptic restricted three-body problem, the picture is the same, but the frame rotates nonuniformly and pulsates isotropically in x and y to ensure that the primary masses remain fixed at the positions $(-\mu, 0)$ and $(1-\mu, 0)$.

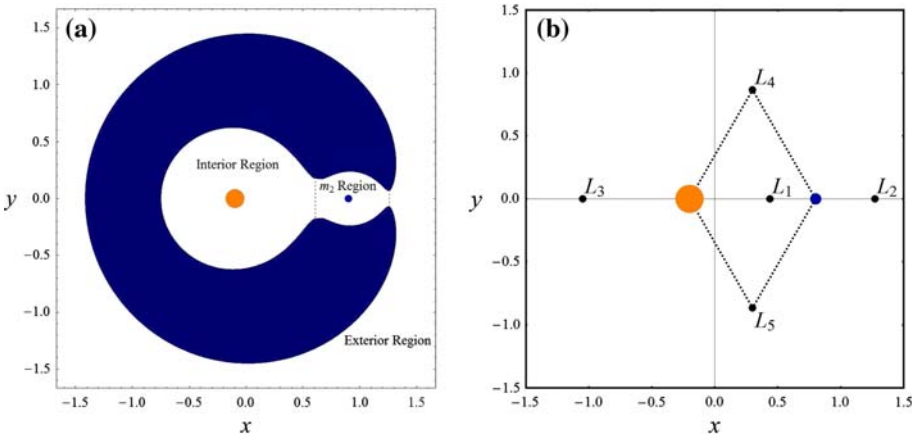

Fig. 2 **a** Regions of allowed motion (*white areas*) in the circular restricted three-body problem with $\mu = 0.1$, $E = -1.775$. **b** Equilibrium points L_i, $i = 1, 2, 3, 4, 5$ in the circular restricted three-body problem with $\mu = 0.1$

is a constant of motion for the CR3BP. We shall refer to this constant as the energy of the system. Throughout this report, $E(L_i)$ shall denote the energy of the ith Lagrange point, i.e. $E(L_i) = E(L_i^x, L_i^y, 0, 0)$. Since E is constant in the CR3BP and $(\dot{x}^2 + \dot{y}^2)$ is a nonnegative quantity, it immediately follows that m_3 is restricted to regions of the (x, y) plane where

$$-\Omega(x, y) \leq E. \tag{5}$$

Moreover, a given particle in the CR3BP is constrained to a three-dimensional energy surface $\mathcal{M} = \{(x, y, \dot{x}, \dot{y}) \mid E(x, y, \dot{x}, \dot{y}) = \text{const.}\}$ defined by its initial energy.

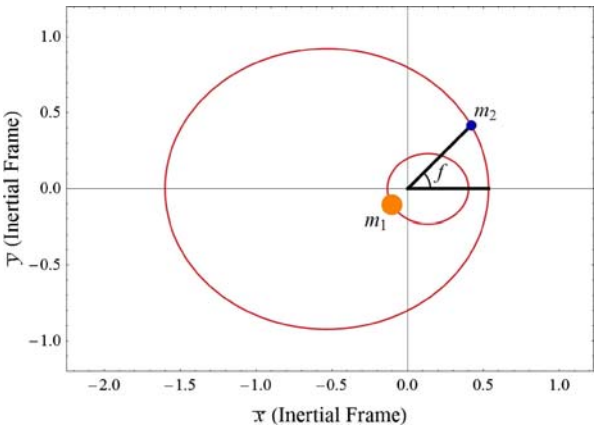

Fig. 3 Elliptical orbits of the primary masses m_1 and m_2 in the ER3BP with respect to an inertial barycentric frame for the case $e = 0.5$, $\mu = 0.2$

1.1.2 The elliptic restricted three-body problem (ER3BP)

A natural generalization of the CR3BP is the elliptic restricted three-body problem (ER3BP), which asks for the motion of a test particle in the presence of two *elliptically* orbiting point masses. In the ER3BP, we introduce the true anomaly $f(t)$, the angle that the line segment joining the rightmost focus of m_2's elliptical orbit to m_2's position at periapsis makes with the line segment joining that focus to m_2's position at time t (see Fig. 3). Normalizing units so that the pair of primary masses has unit angular momentum and the distance between the two primaries at $f = \frac{\pi}{2}$ is unity, it follows from the general solution to the two-body problem (Goldstein et al. 2002) that m_1 and m_2 trace out ellipses given parametrically by

$$(\bar{x}_{m_1}, \bar{y}_{m_1}) = \left(\frac{-\mu}{1 + e\cos f} \cos f, \frac{-\mu}{1 + e\cos f} \sin f \right) \tag{6}$$

$$(\bar{x}_{m_2}, \bar{y}_{m_2}) = \left(\frac{1-\mu}{1 + e\cos f} \cos f, \frac{1-\mu}{1 + e\cos f} \sin f \right), \tag{7}$$

where $(\bar{x}_{m_i}, \bar{y}_{m_i})$, $i = 1,2$ is the position of ith primary mass with respect to an inertial, barycentric coordinate frame.

It can then be shown (Szebehely 1967) that if the true anomaly f is designated the independent variable of the system, then the equations of motion for the elliptic restricted three-body problem take the form

$$\frac{d^2x}{df^2} - 2\frac{dy}{df} = \frac{\partial \Omega}{\partial x} \Big/ (1 + e\cos f) \tag{8}$$

$$\frac{d^2y}{df^2} + 2\frac{dx}{df} = \frac{\partial \Omega}{\partial y} \Big/ (1 + e\cos f), \tag{9}$$

where e is the eccentricity of m_2's elliptical orbit (which is identical to that of m_1's orbit), and x and y are the coordinates of m_3 in a nonuniformly rotating, isotropically pulsating, barycentric coordinate frame in which m_1 and m_2 have fixed positions $(-\mu, 0)$ and $(1-\mu, 0)$, respectively. We shall treat the variable f as the "time" in the ER3BP, but, to avoid ambiguity, shall use primes to denote differentiation with respect to f and dots to denote differentiation

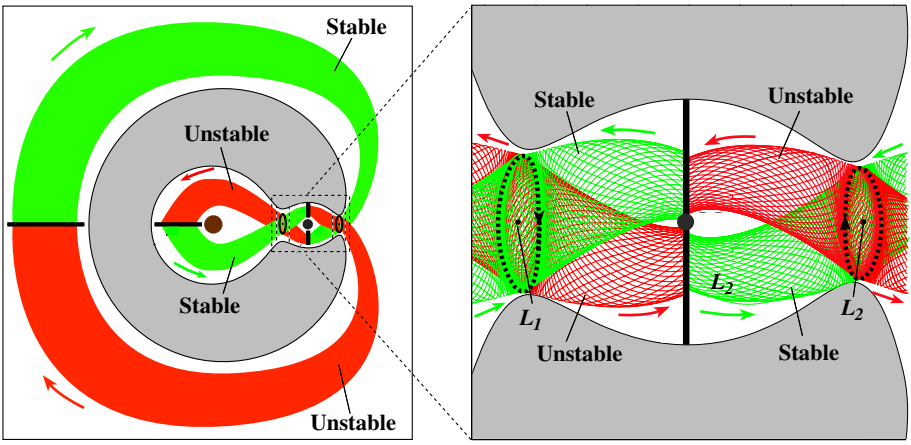

Fig. 4 Projection of the stable (*green*) and unstable (*red*) manifold tubes in the CR3BP onto position space. Image borrowed from Gómez et al. (2001)

with respect to t. Note that when $e = 0$, our choice of units give $f = t$ so that Eqs. 8–9 reduce to the equations of motion (1–2) of the circular restricted three-body problem. Thus, the CR3BP is the special case of the ER3BP in which the two primary masses have zero orbital eccentricity.

1.2 Invariant manifolds

The presence of forbidden regions in the CR3BP permits the definition of three subsets of the (x, y) plane when $E(L_2) < E < E(L_3)$: the interior, m_2, and exterior regions, bounded approximately by the lines $x = L_1^x$, $x = L_2^x$, and the boundary of the forbidden regions (see Fig. 2a). A natural question to pose now is the following: what regulates the transport of particles between the interior, m_2, and exterior regions in the CR3BP?

Koon et al. (2000a), building off of the work of Conley (1968), provide the answer to this question through analysis of the invariant manifolds of periodic orbits in the CR3BP. By linearizing the equations of motion at the collinear Lagrange points, the authors show that these equilibrium points have the stability type $saddle \times center$. Consequently, there exists a family of periodic orbits (called Lyapunov orbits) about L_i for each $i \in \{1, 2, 3\}$, whose stable and unstable manifolds form cylindrical tubes ($S^1 \times \mathbb{R}$). Moreover, within a surface of constant energy, these tubes (as shown in Fig. 4) form codimension-1 separatrices between orbits with different fates: transit orbits, which exit one region and enter an adjacent region; and non-transit orbits, which remain entrapped in the region in which they began. More precisely, a particle with energy E that is currently in a given region R_A will enter an adjacent region R_B under the forward (respectively, backward) time flow if and only if that particle is inside the stable (respectively, unstable) manifold tube emanating from the unique periodic orbit of energy E associated with the Lagrange point that lies on the shared boundary of regions R_A and R_B.

Computational methods for determining the CR3BP invariant manifolds are well-developed (Parker and Chua 1989; Ross 2004). To summarize the procedure, one first constructs a periodic orbit with a specified energy using differential correction. The evolution of the periodic orbit's state transition matrix is computed over one period, and local

approximations of the stable and unstable manifolds of the periodic orbit are obtained from the eigenvectors of that state transition matrix. A set of tracers in the directions of the stable and unstable eigenspaces can then be advected under the full nonlinear equations of motion to generate the invariant manifolds. The process can be curtailed by exploiting a symmetry in the CR3BP equations of motion: the mapping $(x, y, \dot{x}, \dot{y}, t) \mapsto (x, -y, -\dot{x}, \dot{y}, -t)$ is a symmetry of Eqs. 1–2; as a result, the unstable manifold of a given Lyapunov orbit can be found by negating the y and $\dot{x}$ coordinates of every point on the corresponding stable manifold.

1.3 Lagrangian coherent structures (LCS)

The CR3BP invariant manifolds studied in this report are associated with families of periodic solutions of the time-independent equations of motion (1–2). In a non-autonomous dynamical system like the ER3BP, the time-dependence of the flow precludes a direct application of the definition of an invariant manifold to the system and its limit sets. Fortunately, in many non-autonomous dynamical systems, LCS may be viewed as the time-dependent generalizations of static invariant manifolds (Shadden et al. 2005).

For a continuous dynamical system with flow Φ, LCS are defined with respect to the system's finite-time Lyapunov exponent (FTLE) field, a scalar field which assigns to each point $\mathbf{x}$ in the domain a measure $\sigma(\mathbf{x})$ of the rate of divergence of trajectories with neighboring initial conditions about that point:

$$\sigma_{t_0}^{T}(\mathbf{x}) = \frac{1}{|T|} \log \left\| \frac{d\Phi_{t_0}^{t_0+T}(\mathbf{x})}{d\mathbf{x}} \right\|_2 \tag{10}$$

Here, $\left\| \frac{d\Phi_{t_0}^{t_0+T}(\mathbf{x})}{d\mathbf{x}} \right\|_2$ denotes spectral norm of the matrix $\frac{d\Phi_{t_0}^{t_0+T}(\mathbf{x})}{d\mathbf{x}}$, i.e. the square root of the largest eigenvalue of

$$\Delta = \left(\frac{d\Phi_{t_0}^{t_0+T}(\mathbf{x})}{d\mathbf{x}} \right)^{*} \frac{d\Phi_{t_0}^{t_0+T}(\mathbf{x})}{d\mathbf{x}}. \tag{11}$$

Separatrices can be associated with high FTLE values, since neighboring trajectories on opposite sides of a separatrix tend to diverge most quickly. Hence, LCS are defined as *ridges* (curves—or, more generally, codimension-1 surfaces in systems with arbitrary dimension—in the domain whose images in the graph of the FTLE field satisfy certain conditions that formalize intuitive notions of a ridge[1]) in the system's FTLE field. These time-varying ridges form barriers between the almost invariant sets of the domain and can be viewed as the non-autonomous analogues of time-independent invariant manifolds.

To compute LCS in a dynamical system with an n-dimensional phase space, we advect a regularly spaced, n-dimensional, rectilinear grid of tracers forward in time by a fixed length T using numerical integration. (In this study, an adaptive-time stepping Runge–Kutta–Fehlberg routine (RKF45) (Press et al. 1992) was used to integrate tracers.) The results of numerical integration may then be used to compute FTLE values at each point in the rectilinear grid,

[1] For two-dimensional scalar fields $\sigma(\mathbf{x})$, ridges are defined as curves $\mathbf{c}(s)$ in the domain for which two conditions are satisfied: At all points along the curve, (i) $\mathbf{c}'(s)$ and $\nabla\sigma(\mathbf{c}(s))$ are parallel, and (ii) $\langle \hat{\mathbf{n}}, \frac{d^2\sigma}{d\mathbf{x}^2}\hat{\mathbf{n}} \rangle = \min_{||\mathbf{u}||=1} \langle \mathbf{u}, \frac{d^2\sigma}{d\mathbf{x}^2}\mathbf{u} \rangle < 0$, where $\hat{\mathbf{n}}$ is the unit vector normal to the curve $\mathbf{c}(s)$. For further details, the reader is referred to the work of Shadden et al. (2005) and to that of Lekien et al. (2007), where a generalization of these conditions to higher dimensions is also given.

using Eq. 10. Since the matrix $\frac{d\Phi_{t_0}^{t_0+T}(\mathbf{x})}{d\mathbf{x}}$ of Eq. 10 consists of partial derivatives of the form $\frac{\partial[\Phi_{t_0}^{t_0+T}(\mathbf{x})]_i}{\partial x_j}$, where x_i and x_j are components of the state vector $\mathbf{x}$, we calculate these partial derivatives via central differencing of neighboring tracers using the second-order approximation

$$\frac{\partial\left[\Phi_{t_0}^{t_0+T}(\mathbf{x})\right]_i}{\partial x_j} \approx \frac{\left[\Phi_{t_0}^{t_0+T}(\mathbf{x}+\Delta\mathbf{x}_j)\right]_i - \left[\Phi_{t_0}^{t_0+T}(\mathbf{x}-\Delta\mathbf{x}_j)\right]_i}{2\Delta x_j}. \tag{12}$$

Here, $\Delta\mathbf{x}_j = (0, \ldots, 0, \Delta x_j, 0, \ldots, 0)$ denotes the initial separation between the appropriate neighboring tracers in the rectilinear grid.[2] Once computed, the scalar FTLE field may then be plotted, revealing LCS as ridges.

For domains with dimension 2, a contour plot of the FTLE field provides an adequate graphic medium for visualizing LCSs. For the figures displayed in Sect. 3 (where LCSs were extracted from three-dimensional FTLE fields), ridges were extracted manually. To do so, contour plots of two-dimensional cross sections of each three-dimensional FTLE field were generated, and for each cross section, the ridge of interest was traced out manually with a sequence of points. The accumulation of selected points was then plotted as an interpolated surface.

The use of finite differencing (as opposed to integration of the system's variational equations) for LCS computation is largely a pragmatic choice. Since a grid of tracers must be advected to obtain the scalar FTLE field, obtaining the numerical value of $\frac{d\Phi_{t_0}^{t_0+T}(\mathbf{x})}{d\mathbf{x}}$ at each point on the grid becomes a simple matter of subtraction and division, circumventing the computational costs of integrating extra differential equations for the components of $\frac{d\Phi_{t_0}^{t_0+T}(\mathbf{x})}{d\mathbf{x}}$. Additionally, Shadden et al. (2005) point out that finite differencing may unveil LCS more reliably than obtaining derivatives of the flow analytically, owing to the possibility that the theoretical value of the FTLE at a point lying close to, but not precisely on, an LCS may be quite small; finite differencing can often opportunely overapproximate the FTLE at such points, provided one or more of its neighbors lies opposite the LCS.

Note that (10) permits the computation of a backward-time FTLE through the use of a negative integration length T. A ridge in such a backward-time FTLE field (which we distinguish from forward-time FTLE ridges with the names *attracting LCS* for the former, *repelling LCS* for the latter) corresponds to the time-dependent analogue of an unstable manifold. A symmetry in the ER3BP equations of motion, akin to the CR3BP symmetry described previously, eliminates the need to compute backward-time FTLE fields: noting that the cosine function is an even function, it is easy to check that the mapping $(x, y, x', y', f) \mapsto (x, -y, -x', y', -f)$ is a symmetry of Eqs. 8–9; as a result, any attracting LCS in the ER3BP can be found by negating the y and x' coordinates of every point on the corresponding repelling LCS and viewing its evolution in reverse time. Moreover, Eqs. 8–9 are periodic with period 2π. Thus, the LCS in the ER3BP need only be computed over the interval $0 \leq f < 2\pi$; an LCS at any other epoch $\tilde{f}$ can be identified with the LCS at the time $f \in [0, 2\pi)$ congruent to $\tilde{f}$ modulo 2π.

[2] Initial separation distances are predetermined by one's choice of grid resolution together with the bounds of the domain under examination. In this study, grid resolutions of 250×250 in the variables $(x, \dot{x})$ were used to generate Figs. 6 and 7; grid resolutions of $100 \times 100 \times 60$ in the variables (x, x', E) were used to generate Figs. 9, 11, 13 and 14; and grid resolutions of 250×250 and 100×100 in the variables (y, y') were used to generate Figs. 15 and 16, respectively. (Separation distances in the remaining unplotted variables were chosen to lie at or below the average separation distance of the corresponding plotted variables.)

On that note, it is worth mentioning that the periodicity of the ER3BP equations of motion (8–9) means that one could, in principle, obtain the results presented in this report using standard manifold globalization techniques. Indeed, consider the map $\Phi_{f_0}^{f_0+2\pi}$, where Φ denotes the flow of Eqs. 8–9 and $f_0 \in [0, 2\pi)$ is a fixed true anomaly. This map defines a discrete dynamical system on the Poincaré section $U_{f_0} = \{(x, y, x', y', f) \mid f = f_0\}$ of the ER3BP's augmented phase space. Using the methods of Parker and Chua (1989), one could extract invariant manifolds from U_{f_0} for a series of initial epochs f_0 and conceivably replicate the LCS animations presented in this report. The reader should bear in mind, however, that there are more general situations (e.g., the four-body problem in the case where the ratio of the periods of the two smaller primary masses is irrational) in which LCS analysis applies even though the aperiodicity of the flow eliminates the possibility of using the method just described.

2 Computational methodology

A key obstacle encumbering the investigation of LCS in the elliptic restricted three-body problem (ER3BP) is the dimension of the system under examination. In contrast to the CR3BP, where the existence of a constant of motion restricts the motion of the test particle to a three-dimensional energy surface within which there exist cylindrical invariant manifolds, the ER3BP possesses no integrals of motion. Thus, any LCS in the ER3BP is formally a three-dimensional surface contained in the ER3BP's four-dimensional phase space. As an extraction and visualization of such a structure would be difficult, we explore two means of circumventing this obstacle.

2.1 Poincaré maps and the finite-iteration Lyapunov exponent

One such method utilizes Poincaré sections to reduce the dimension of the system by one. Selecting a three-dimensional hyperplane $U \subset \mathbb{R}^4$ and seeding a subset $U_0 \subset U$ with a grid of tracers, we can advect these tracers under the flow until their orbits' (directed) Nth intersections with the hyperplane are reached. It then becomes feasible to compute (in the manner described in Sect. 1.3) a finite-iteration Lyapunov exponent (FILE)

$$\sigma^N(\mathbf{x}) = \frac{1}{|N|} \log \left\| \frac{d\mathbf{P}^N(\mathbf{x})}{d\mathbf{x}} \right\| \tag{13}$$

for each point $\mathbf{x} \in U_0$, where the function $\mathbf{P} : U \to U$ is the one-sided Poincaré map associated with the plane U and the flow Φ of Eqs. 8–9. We shall refer to this method as the Poincaré map method, its associated field being an FILE field.

2.2 The finite-time Lyapunov exponent

Alternatively, it is possible to compute four-dimensional FTLE fields (in the manner described in Sect. 1.3) and examine three-dimensional cross sections of these fields. We shall refer to this method as the cross-sectional method, its associated field being an FTLE field.

2.3 A comparison using the circular restricted three-body problem (CR3BP) as a test bed

In order to gauge the performance of these two methods, we first apply them to a simpler, lower dimensional system, namely the CR3BP equations of motion with a fixed energy E.

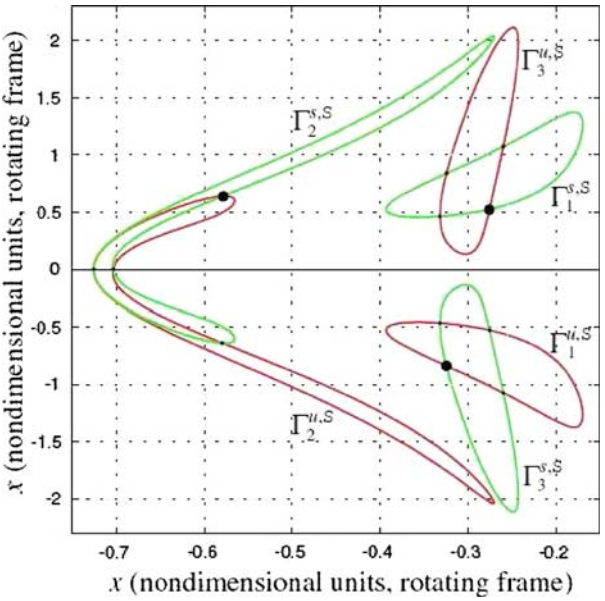

Fig. 5 Intersection of the stable (*green*) and unstable (*red*) manifold tubes in the CR3BP with the plane $y = 0$ (within a surface of constant energy). Here $\mu = 0.1$ and $E = E(L_1) + 0.03715$. The labels $\Gamma_i^{s,\mathrm{S}}$ and $\Gamma_i^{u,\mathrm{S}}$ denote the ith intersections of the stable and unstable manifolds, respectively, of the L_1 Lyapunov orbit with the plane $y = 0$ in the interior region within a surface of constant energy. (The capital S in $\Gamma_i^{s,\mathrm{S}}$ and $\Gamma_i^{u,\mathrm{S}}$ specifies that the intersection lies in the interior, or "Sun," region.) Image borrowed from Koon et al. (2000a)

Since the invariant manifolds of the CR3BP are examined in considerable detail by Koon et al. (2000a), it helps to compare the outputs of the two methods with published data. Figure 5, taken from Koon et al. (2000a), shows the intersection of the stable and unstable manifold tubes of the Lyapunov orbit about L_1 for a fixed energy just above $E(L_1)$. Throughout this report, we adopt the notation of Koon et al. (2000a): $W^s_{L_1,\mathrm{p.o.}}$ and $W^u_{L_1,\mathrm{p.o.}}$ denote the stable and unstable manifolds, respectively, of the L_1 Lyapunov orbit, and $\Gamma_i^{s,\mathrm{S}}$ and $\Gamma_i^{u,\mathrm{S}}$ denote the ith intersection of $W^s_{L_1,\mathrm{p.o.}}$ and $W^u_{L_1,\mathrm{p.o.}}$, respectively, with the plane $y = 0$ in the interior region within a surface of constant energy. (The capital S in $\Gamma_i^{s,\mathrm{S}}$ and $\Gamma_i^{u,\mathrm{S}}$ specifies that the intersection lies in the interior, or "Sun," region.)

Figure 6a plots the CR3BP FTLE field along the plane $y = 0$ (within a surface of constant energy) for an integration time $T = 2$, as computed using the cross-sectional method. As expected, large FTLE values can be observed at the first intersection $\Gamma_1^{s,\mathrm{S}}$ of the stable manifold $W^s_{L_1,\mathrm{p.o.}}$ of the L_1 Lyapunov orbit. Increasing the integration time T (Fig. 6b) unveils the subsequent intersection $\Gamma_2^{s,\mathrm{S}}$ of the same stable manifold.

For comparison, the FILE field for the first three iterations of the Poincaré map associated with the plane $y = 0$ (within a surface of constant energy) are shown in Fig. 7. In analogy with increasing integration time, increasing the iteration number N successively unveils the higher order intersections $\Gamma_1^{s,\mathrm{S}}$, $\Gamma_2^{s,\mathrm{S}}$, and $\Gamma_3^{s,\mathrm{S}}$ of $W^s_{L_1,\mathrm{p.o.}}$ with the plane $y = 0$.

Notice that the FILE field has a significant drawback: in addition to locating transport barriers associated with stable manifolds of limit sets, the FILE field also exhibits ridges where the Poincaré map is not differentiable due to a lack of transversality between orbits and the plane of interest. Indeed, for initial points on the Poincaré section whose orbits do not intersect the surface of section transversally upon their return, differentiability is not guaranteed and the FILE loses its meaning. Unfortunately, for a given FILE field, these structures appear indistinguishably from genuine transport barriers and bear little or no influence on the dynamics of the system. Furthermore, the Poincaré map $\mathbf{P}$ is in general only defined for

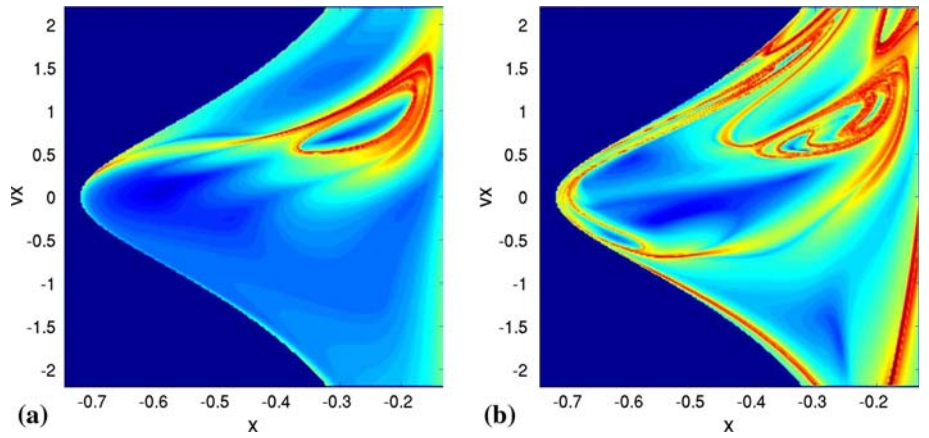

Fig. 6 FTLE field contour plot (i.e., generated using a cross-sectional FTLE calculation) in the CR3BP (within a surface of constant energy) at the plane $y = 0$ with integration time **a** $T = 2$ and **b** $T = 5$. Energy and mass parameters are identical to those in Fig. 5. Observe that increasing integration time reveals the second intersection $\Gamma_2^{s,\mathrm{S}}$ of the stable manifold of the L_1 Lyapunov orbit, as well as some additional curves of high FTLE

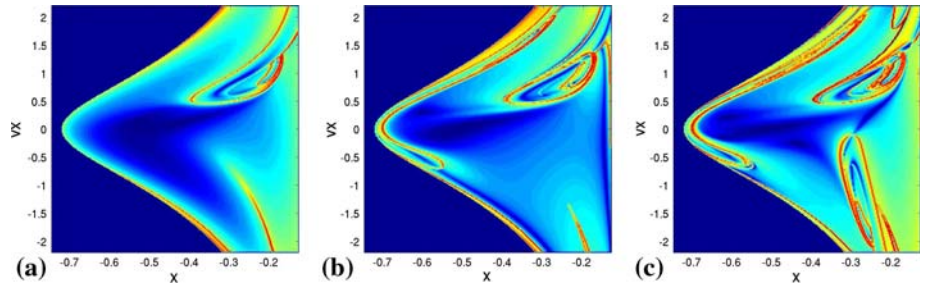

Fig. 7 FILE field contour plot (i.e., generated using a Poincaré map calculation) in the CR3BP (within a surface of constant energy) at the plane $y = 0$ for iterations **a** $N = 1$, **b** $N = 2$, and **c** $N = 3$. Again, energy and mass parameters are identical to those in Fig. 5. Notice the superfluous FILE ridges caused by a lack of transversality between orbits and the surface of section in, for instance, the lower right-hand corners of (**a**) and (**b**). Unsurprisingly, larger iteration numbers N reveal the higher order intersections $\Gamma_2^{s,\mathrm{S}}$ and $\Gamma_3^{s,\mathrm{S}}$ of the stable manifold of the L_1 Lyapunov orbit

a subset of the surface of section U. For these reasons, we have adopted the cross-sectional method as the standard for all subsequent computations.

3 Lagrangian coherent structures in the planar elliptic restricted three-body problem (ER3BP)

The computational tools developed in the previous section make possible the presentation of the main results of this study, LCS in the planar elliptic restricted three-body problem (ER3BP). Recall that in the ER3BP, whose equations of motion are non-autonomous and possess no integrals of motion, the notions of constant-energy surfaces lose their relevance,

and hence we must examine the time-dependent analogues of $W^s_{L_1,\text{p.o.}}$ and $W^u_{L_1,\text{p.o.}}$ in the full four-dimensional phase space, where the plane $y = 0$ is three-dimensional. An important question to ask at this moment is the following: What will the intersection of $W^s_{L_1,\text{p.o.}}$ with plane $y = 0$ in the interior region look like? The answer to this question depends crucially on our choice of coordinate system.

Let

$$E(x, y, x', y') = \frac{1}{2}(x'^2 + y'^2) - \frac{\Omega}{1 + e\cos f}, \tag{14}$$

where, in the notation mentioned previously, x' and y' have been used to denote the quantities $\frac{dx}{df}$ and $\frac{dy}{df}$, respectively. Notice that when $e = 0$, (14) reduces to the expression for the energy in the CR3BP given in Eq. 4. We shall refer to this quantity as the "energy" in the ER3BP, with the hopes that this notation will give the reader a better sense of the correlation between the quantities defined here and their CR3BP analogues. In actuality, (14) is the ER3BP's Hamiltonian.

Choosing a coordinate system (x, y, x', E) to parametrize phase space in the ER3BP (so that the plane $y = 0$ is parametrized by x, x', and E) allows for a natural means of extending the qualitative results of LCS studies in the CR3BP. For fixed values of E at the plane $y = 0$, $x < 0$, a ridge in the FTLE field on the $(x, x', y = 0, E = \text{const.})$ plane should appear as a closed curve, corresponding to a perturbed version of $\Gamma_1^{s,S}$ (the perturbation arising from the fact that the eccentricity e is nonzero). Since the amplitude of an L_1 Lyapunov orbit in the CR3BP is roughly proportional to the square root of its energy minus $E(L_1)$, we should expect that this closed curve will shrink with decreasing E and that for some critical energy the curve will contract to a point. Consequently, the intersection of the LCS with the plane $y = 0$ might appear as a distorted paraboloid, provided we parametrize phase space with the coordinates x, y, x', and E. See Fig. 8 for an illustration of this notion.

3.1 A test case

Figure 9 displays snapshots of the intersection of the plane $y = 0$ with the LCS corresponding to the analogue of $W^s_{L_1,\text{p.o.}}$ under a set of fabricated parameters (mass ratio $\mu = 0.1$, orbital eccentricity $e = 0.04$). The video http://www.its.caltech.edu/~egawlik/ER3BPLCS/LCS-ER3BP.mov (files can be downloaded from our site) shows the full sequence of images in animated format. The LCS was extracted from an FTLE field generated by advecting tracers over an integration length $T = 2.5$, roughly $\frac{2}{5}$ of the orbital period of the two primary masses. As expected, the LCS forms a distorted paraboloid that pulsates with time. The key property of this LCS is that, like $W^s_{L_1,\text{p.o.}}$ of the CR3BP, this LCS separates orbits that enter m_2's "sphere of influence" from orbits that do not.

To help visualize the role that this LCS plays in the dynamics of the ER3BP, Fig. 10 displays snapshots of the motion of a collection of tracers that have been colored based upon their initial location relative to the LCS. The tracers were seeded at true anomaly $f = \pi/2$ over a $15 \times 15 \times 15$ (x, x', E) grid on the plane $y = 0$ and advected forward in time. Blue tracers began inside the LCS "bowl," while red tracers began outside the LCS "bowl." The video http://www.its.caltech.edu/~egawlik/ER3BPLCS/Tracers.avi (files can be downloaded from our site) shows the full sequence of images in animated format.

Notice that even in the absence of precise boundaries delineating the interior, m_2, and exterior regions of the ER3BP, a clear dichotomy exists among orbits in the vicinity of m_1 headed toward the L_1 equilibrium region: Orbits contained in the LCS analogue of $W^s_{L_1,\text{p.o.}}$ (the blue tracers of http://www.its.caltech.edu/~egawlik/ER3BPLCS/Tracers.avi) are tempo-

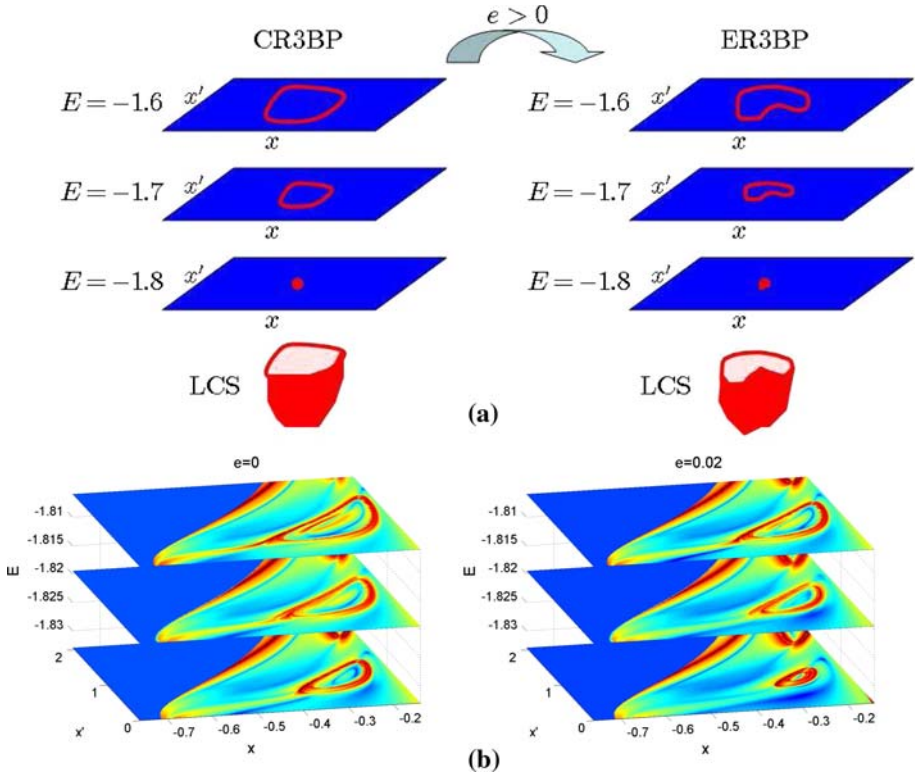

Fig. 8 **a** Schematic illustration of the hypothesis that, in terms of the coordinates x, y, x', and E, the intersection of the plane $y = 0$ with the LCS corresponding to the analogue of $W^s_{L_1,\text{p.o.}}$ might appear as a distorted paraboloid in the ER3BP. **b** A pair of FTLE field contour plots verifying the distorted paraboloid hypothesis. The left plot displays slices of the FTLE field computed along the plane $y = 0$ in the CR3BP with mass ratio $\mu = 0.1$ (and, by definition, orbital eccentricity $e = 0$), while the right plot displays slices of the FTLE field at the same location in the ER3BP with mass ratio $\mu = 0.1$ and nonzero orbital eccentricity $e = 0.02$. Further analysis of this phenomenon is given in Sect. 3.3

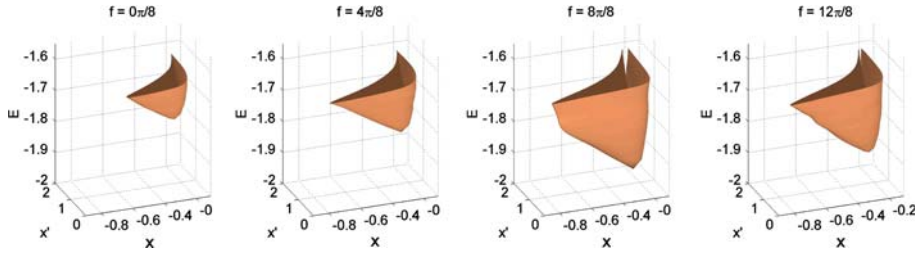

Fig. 9 Intersection of the plane $y = 0$ with the LCS corresponding to the time-dependent analogue of $W^s_{L_1,\text{p.o.}}$ in the ER3BP with mass ratio $\mu = 0.1$, orbital eccentricity $e = 0.04$. See http://www.its.caltech.edu/~egawlik/ER3BPLCS/LCS-ER3BP.mov (files can be downloaded from our site) to view the full sequence of images in animated format

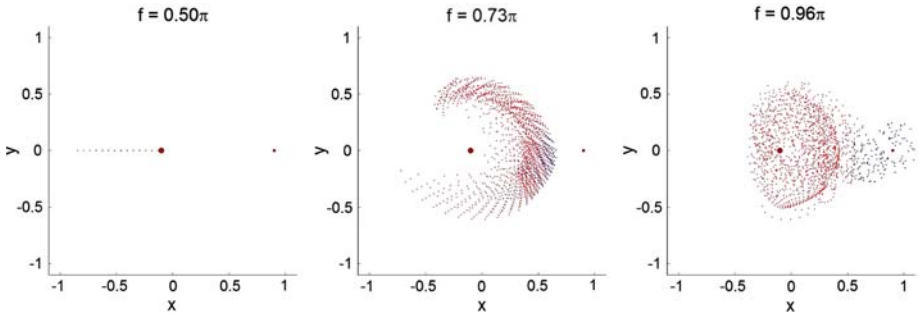

Fig. 10 Snapshots of the motion of a collection of tracers colored based upon their initial location relative to the LCS in Fig. 9. The tracers were seeded at true anomaly $f = \pi/2$ over a $15 \times 15 \times 15(x, x', E)$ grid on the plane $y = 0$ and advected forward in time. Blue tracers began inside the LCS "bowl," while red tracers began outside the LCS "bowl." See http://www.its.caltech.edu/~egawlik/ER3BPLCS/Tracers.avi (files can be downloaded from our site) to view the full sequence of images in animated format

rarily captured at m_2, while orbits exterior to the LCS analogue of $W^s_{L_1,\text{p.o.}}$ (the red tracers of http://www.its.caltech.edu/~egawlik/ER3BPLCS/Tracers.avi) remain entrapped in the interior region. In addition, numerical experiment reveals that tracers lying identically on the LCS analogue of $W^s_{L_1,\text{p.o.}}$ tend toward quasiperiodic orbits about the ER3BP's L_1 equilibrium point. Similar phenomena related to the asymptotic behavior of points comprising an LCS are observed in the ensuing section on LCS in the Sun–Mercury system (see Sect. 3.4). In succinct terms, the ER3BP LCS studied in this report fill the role of the CR3BP's collection of invariant manifolds emanating from the L_1 and L_2 equilibrium regions. The LCS partition the ER3BP phase space, regulate the flow of particles between the (ill-defined) interior, m_2, and exterior regions of position space, and comprise trajectories with exceptional limiting behavior.

The degree to which LCSs act as dynamical barriers in the ER3BP can be measured quantitatively. It was earlier mentioned that under suitable conditions, a time-dependent dynamical system's LCS may be justifiably viewed as nearly invariant manifolds; that is, the LCSs behave as nearly material surfaces which admit negligible flux under the system's flow. This can be verified for the LCS of Fig. 9 by computing the quantity

$$\gamma(\mathbf{x}) = \left\langle \hat{\mathbf{n}}, \frac{d^2\sigma}{d\mathbf{x}^2}\hat{\mathbf{n}} \right\rangle \tag{15}$$

along the LCS, which is a measure of the curvature of the ridge (recall that LCSs are ridges in the system's Finite Time Lyapunov Exponent Field $\sigma(\mathbf{x})$) in its normal direction expressed in terms of the domain's FTLE field $\sigma(\mathbf{x})$ and the unit normal vector $\hat{\mathbf{n}}$ to the ridge at the point $\mathbf{x}$. γ gauges how well-defined the ridge is at the point $\mathbf{x}$ and can be shown to bear an inverse relationship with the flux across the LCS (Lekien et al. 2007). Numerical differentiation of the scalar field $\sigma(\mathbf{x})$ reveals that for the LCS of Fig. 9, typical values of γ along the LCS are on the order of 10^4, a number on the same order of magnitude as the values reported by Lekien et al. (2007) for a sample three-dimensional dynamical system with an LCS whose flux admittance is negligible. Similar ridge curvature values are found for the LCSs in the subsequent sections of this report, indicating that the LCSs in the elliptic restricted three-body problem may indeed be viewed as nearly invariant manifolds that act as material barriers.

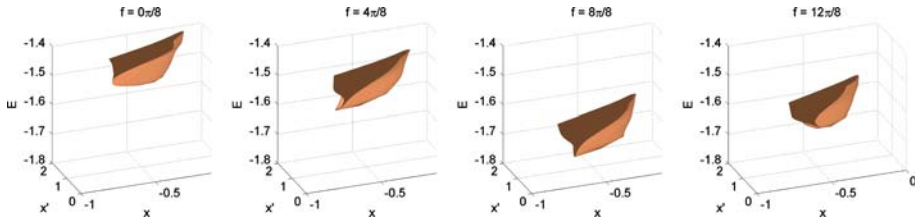

Fig. 11 Intersection of the plane $y = 0$ with the LCS corresponding to the time-dependent analogue of $W^s_{L_1,\text{p.o.}}$ in the Earth–Moon–spacecraft system (mass ratio $\mu \approx 0.012$, orbital eccentricity $e \approx 0.055$). See http://www.its.caltech.edu/~egawlik/ER3BPLCS/LCS-ER3BP-Earth-Moon.mov (files can be downloaded from our site) to view the full sequence of images in animated format

3.2 LCS in the Earth–Moon system

The Earth–Moon–spacecraft system (mass ratio $\mu \approx 0.012$, orbital eccentricity $e \approx 0.055$) provides an excellent physical system for which ER3BP LCSs can be examined. Figure 11 (along with an animated version in the video http://www.its.caltech.edu/~egawlik/ER3BPLCS/LCS-ER3BP-Earth-Moon.mov (files can be downloaded from our site)) displays an LCS in the Earth–Moon–spacecraft ER3BP. To facilitate comparison with the results presented in Sect. 3.1, we have computed the intersection of the plane $y = 0$ with the LCS corresponding to the analogue of $W^s_{L_1,\text{p.o.}}$ in the Earth–Moon–spacecraft ER3BP, this time using an integration length $T = 3.5$. In this case, the LCS encloses a smaller fraction of phase space than the LCS of Sect. 3.1, which is to be expected given the lower mass ratio μ in the Earth–Moon system.

As an ex post facto motivation for analysis of LCS in this system, we note in passing that past studies have demonstrated that invariant manifolds in the Earth–Moon–spacecraft CR3BP can serve as useful building blocks for the design of low-fuel trajectories for Earth-to-Moon missions. Koon et al. (2000b) have shown that linking a trajectory that shadows the invariant manifolds of a Sun–Earth L_2 Lyapunov orbit in sequence with a trajectory enclosed by the stable manifold tube of an Earth–Moon L_2 Lyapunov orbit can generate an Earth-to-Moon trajectory that requires little fuel for mid-course maneuvers. In Fig. 12, we show an example of such a trajectory in a Sun–Earth rotating coordinate frame. After departure from a low Earth parking orbit, a trajectory like the one plotted can require as little as 34 m/s (plus an initial Earth-orbit departure ΔV) to travel to the Moon and achieve ballistic capture at the Moon (Koon et al. 2000b). Such trajectories, which bear a close connection with so-called weak stability boundary (WSB) regions of the Sun–Earth–spacecraft CR3BP (Garcia and Gómez 2007), can be shown to provide fuel savings for Earth-to-Moon transfers of 10–110 m/s relative to a standard Hohmann transfer approach (Perozzi and Di Salvo 2008). The fuel savings of Fig. 12, of course, come at a cost: while a classic Hohmann transfer from a low-Earth parking orbit to an orbit about Earth with radius matching that of the Moon takes just 5 days to execute (Kemble 2006), the trajectory in Fig. 12 has a flight time of roughly 6 months. Nevertheless, trajectories like that of Fig. 12 might be well-suited for certain missions in which short flight times may be more safely sacrificed for fuel savings.

3.3 LCS dependence on the mass parameter μ and the orbital eccentricity e

Sections 3.1 and 3.2 and the figures therein suggest a dependence of ER3BP LCS on the two dimensionless parameters which characterize the ER3BP: the orbital eccentricity e of

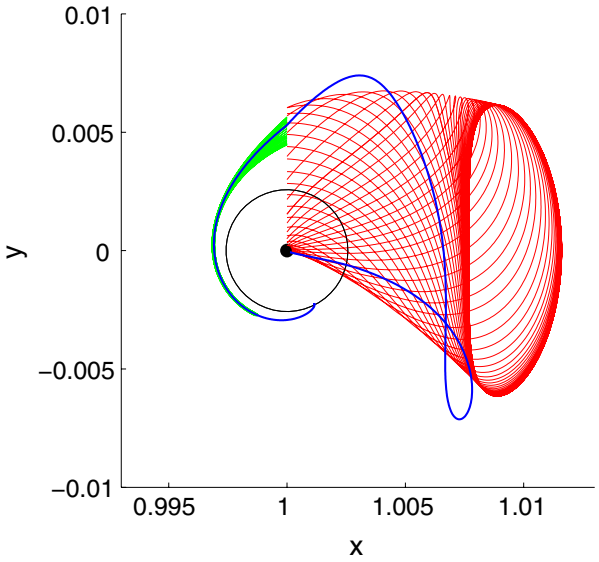

Fig. 12 Fuel-efficient Earth-to-Moon trajectory juxtaposed with the Sun–Earth (*red*) and Earth–Moon (*green*) invariant manifolds, in Sun–Earth rotating coordinates that have been normalized so that the Sun–Earth distance is unity. The central black disc denotes the Earth, while the thin black circle traces the Moon's orbit. The red tube is the unstable manifold of a Sun–Earth L_2 Lyapunov orbit; the green tube is the stable manifold of an Earth–Moon L_2 Lyapunov orbit. After departure from a low Earth parking orbit, a trajectory like the one plotted above can require as little as 34 m/s beyond initial Earth-orbit departure costs to travel to the Moon and achieve temporary capture at the Moon (Koon et al. 2000b)

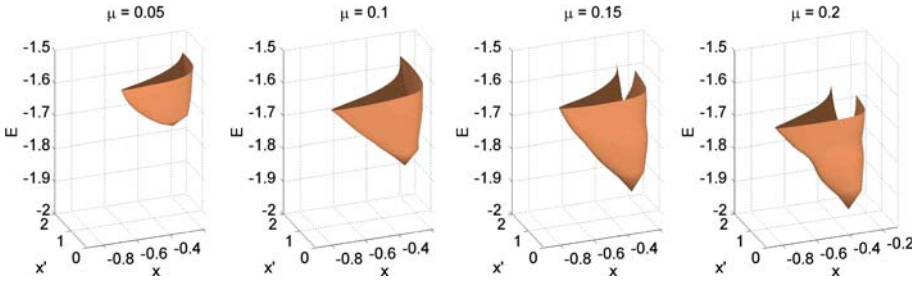

Fig. 13 Dependence of a Lagrangian coherent structure on the mass parameter μ. The LCS shown is the intersection of the plane $y = 0$ with the LCS corresponding to the time-dependent analogue of $W^s_{L_1,\text{p.o.}}$ at epoch $f = \pi/2$ in the elliptic restricted three-body problem with fixed orbital eccentricity $e = 0.04$

the primary masses and their mass ratio μ. In this section, we examine this dependence systematically. Figures 13 and 14 illustrate the evolution of an LCS in the ER3BP under variations of e and μ, respectively. Once again, to facilitate comparison with Sects. 3.1–3.2, the LCS shown in the both figures is the intersection of the plane $y = 0$ with the time-dependent analogue of $W^s_{L_1,\text{p.o.}}$ at epoch $f = \pi/2$, here computed using an integration length $T = 2.5$.

Fixing e and examining the evolution of the LCS with increasing μ, we see that the LCS expands in girth and its base lowers in energy, enveloping a larger fraction of the ER3BP phase space as μ grows. This dependence on the mass parameter is physically sensible and reflects the fact that a larger primary mass m_2 exerts a stronger gravitational force on the test particle m_3.

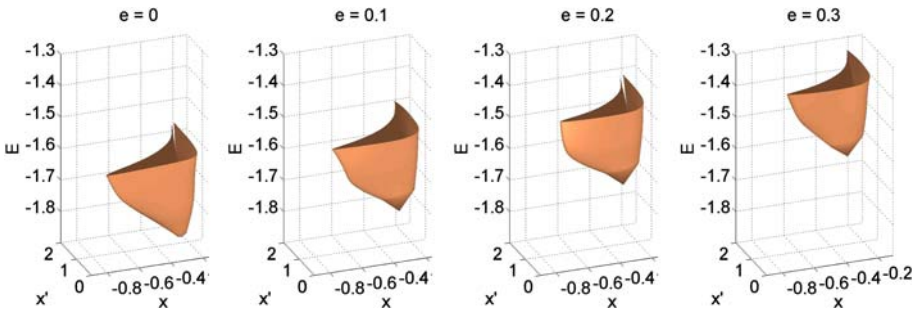

Fig. 14 Dependence of a Lagrangian coherent structure on the orbital eccentricity e. The LCS shown is the intersection of the plane $y = 0$ with the LCS corresponding to the time-dependent analogue of $W^s_{L_1,\text{p.o.}}$ at epoch $f = \pi/2$ in the elliptic restricted three-body problem with fixed mass ratio $\mu = 0.1$

For fixed μ (Fig. 14), LCS evolution with increasing eccentricity is characterized primarily by vertical translation in the energy E. For this particular LCS, increasing the eccentricity raises the minimum energy (given by the energy of the base of LCS "bowl") required for entrance into the m_2 region. This dependence of the LCS on the eccentricity e agrees with the physical intuition that a particle destined to make its next closest pass with m_2 during the interval $\pi/2 < f < 3\pi/2$ (which is the case for the virtually all points composing the phase-space plane under consideration[3]) is less likely to escape the interior region if the eccentricity of m_2's orbit (and hence its non-normalized distance from the origin during the interval $\pi/2 < f < 3\pi/2$) is large.

By examining the evolution of the LCS with increasing eccentricity, we have implicitly illustrated an instance of a general property of LCSs in the ER3BP: namely, LCSs of the ER3BP are continuous deformations of their time-independent analogues in the corresponding CR3BP system (obtained by setting $e = 0$). This corroborates the hypothesis of Fig. 8 and lends evidence to the notion that the role that LCSs play in the dynamics of the ER3BP largely parallels that of the CR3BP invariant manifolds of Fig. 4.

3.4 Mercury and the BepiColombo mission

The planet Mercury embodies the necessity of the use of the elliptic restricted three-body approximation over the circular restricted three-body approximation in the simulation of certain celestial systems. With a value slightly larger than 0.2, Mercury's orbital eccentricity is more than twice that of any other planet in the solar system (Yeomans 2007). It follows that the design of a Mercury-bound space mission relies heavily on ER3BP dynamics. Indeed, the European Space Agency's (ESA) BepiColombo mission, a mission to Mercury scheduled to launch in 2013, intends to utilize solar perturbations to achieve Mercurial capture of the spacecraft (Jehn et al. 2004). Naturally, one might expect such a trajectory to share an intimate connection with LCS in the Sun–Mercury–spacecraft ER3BP. As the following discussion reveals, this intuition is correct.

Figure 15 displays the FTLE field at a cross section of phase space in the spatial elliptic restricted three-body problem (with Sun–Mercury–spacecraft parameters), juxtaposed with

[3] Refer back to Fig. 10 and the accompanying animation http://www.its.caltech.edu/~egawlik/ER3BPLCS/Tracers.avi (files can be downloaded from our site) for a confirmation of this observation.

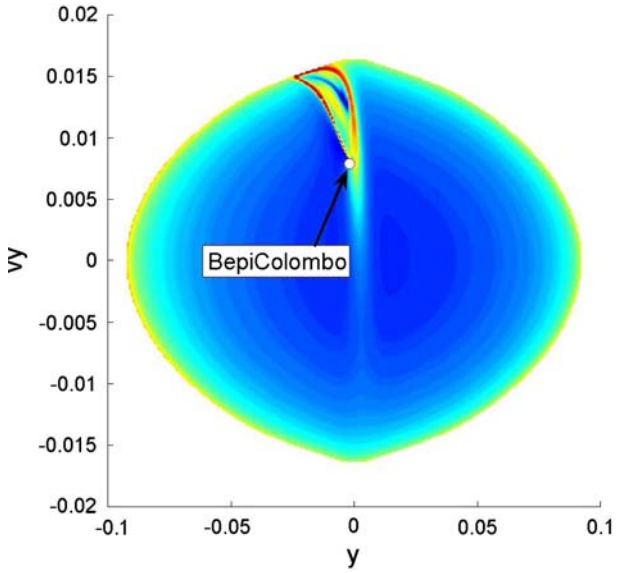

Fig. 15 Snapshot of the FTLE field at a cross section of phase space in the spatial elliptic restricted three-body problem (with Sun–Mercury–spacecraft parameters), juxtaposed with the intersection of BepiColombo's trajectory with that cross section

the intersection of ESA's BepiColombo trajectory[4] with that cross section. Specifically, the cross section shown is the plane $x = 0.99$, $z = 0.0007$, $z' = -0.0003$, $E = -1.7613$ at epoch $f = 3.9065$ in normalized units, which is to the left of the Sun-Mercury L_1 (See Fig. 17 for an illustration). Note that we have worked with the spatial ER3BP (Szebehely 1967) rather than the planar ER3BP for this computation to account for the nonplanarity of BepiColombo's orbit.[5] The LCS seen in Fig. 15 is the time-dependent analogue of the stable manifold of the L_1 Lyapunov orbit in the circular restricted three-body problem, computed using an integration length $T = 2.5$. Notice the remarkable manner in which BepiColombo's trajectory

[4] Baseline trajectory for launch in 2012 (Jehn et al. 2004).

[5] In the case of the spatial ER3BP, Eqs. 8–9 generalize to

$$\begin{aligned} x'' - 2y' &= \frac{\partial \tilde{\Omega}}{\partial x} \Big/ (1 + e\cos f) \\ y'' + 2x' &= \frac{\partial \tilde{\Omega}}{\partial y} \Big/ (1 + e\cos f) \\ z'' + z &= \frac{\partial \tilde{\Omega}}{\partial z} \Big/ (1 + e\cos f), \end{aligned}$$

where

$$\tilde{\Omega}(x, y, z) = \frac{x^2 + y^2 + z^2}{2} + \frac{1-\mu}{\sqrt{(x+\mu)^2 + y^2 + z^2}} + \frac{\mu}{\sqrt{(x-1+\mu)^2 + y^2 + z^2}} + \frac{1}{2}\mu(1-\mu) \qquad (16)$$

and (x, y, z) denotes the position of m_3 with respect to the nonuniformly rotating, isotropically pulsating, barycentric coordinate frame in which m_1 and m_2 have fixed positions $(-\mu, 0, 0)$ and $(1-\mu, 0, 0)$, respectively (Szebehely 1967).

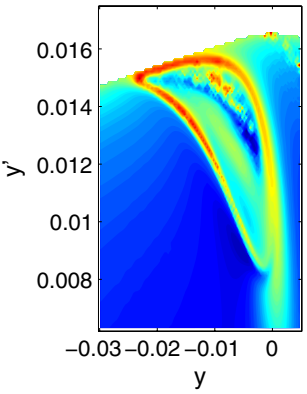

Fig. 16 Magnified view of the FTLE field shown in Fig. 15, this time computed in a full ephemeris model. Note the similarity of this LCS to that of Fig. 15

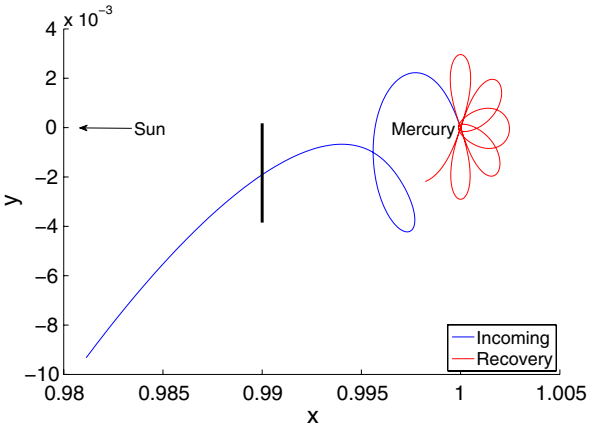

Fig. 17 BepiColombo's ballistic arrival trajectory (baseline trajectory for launch in 2012 (Jehn et al. 2004) in the ER3BP coordinate frame, projected onto the x–y plane. By exploiting solar perturbations, the trajectory nearly winds onto a quasiperiodic orbit about the Sun–Mercury L_1 Lagrange point, is ballistically captured at Mercury, and is subsequently presented with three opportunities for recovery maneuvers in the event of an orbit insertion failure (Jehn et al. 2004). The *vertical black line segment* represents the location of the cross section used in Fig. 15

straddles the LCS. This should come as no surprise, given that this particular LCS governs transport between the interior (Sun) region and the m_2 (Mercury) region.

To validate the use of the elliptic restricted three-body problem as a model for the simulation of trajectories in the Sun-Mercury system, we have recomputed the LCS displayed in Fig. 15 using a full ephemeris model based on Mercurial ephemeris data obtained from the JPL HORIZONS Ephemeris System (Giorgini et al. 1996). The recomputed LCS, shown in Fig. 16, is nearly indistinguishable from the LCS computed in the ER3BP model, verifying the validity of the ER3BP approximation for this celestial system.

The advantages associated with an exploitation of dynamical structures like invariant manifolds and LCS for space mission design are evidenced by the favorable properties of the BepiColombo trajectory (see Fig. 17): In contrast to a classical hyperbolic approach trajectory (Campagnola et al. 2003), the BepiColombo trajectory (baseline trajectory for launch in 2012 (Jehn et al. 2004)) avoids the prospect of a single-point failure during Mercury Orbit Insertion (MOI). By utilizing solar perturbations, the BepiColombo trajectory attains weak capture at the planet and is subsequently presented with three extra MOI opportunities (Jehn et al. 2004). While the difference in total ΔV costs (the combined costs of interplanetary and orbit insertion phases of the mission) between a classical approach and weak capture approach are negligible (Campagnola et al. 2006), the additional recovery opportunities made possible through exploitation of three-body dynamics are certainly advantageous.

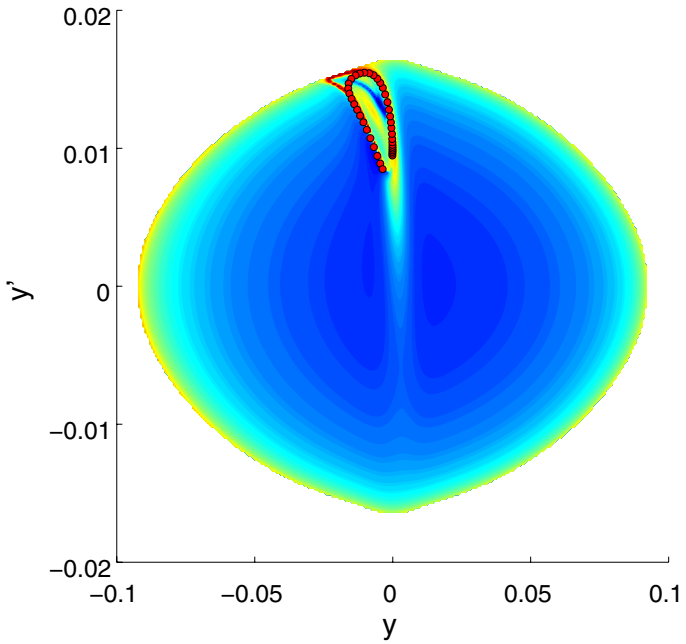

Fig. 18 FTLE field of Fig. 15 superposed with the projection of the $x = 0.99$ Poincaré cut of an ER3BP L_1 Lissajous orbit's stable "pseudo-manifold." The red points belong to a family of trajectories which, under the forward time flow, wind onto a quasiperiodic orbit about the Sun–Mercury L_1. Notice that the LCS and the points lying on the "pseudo-manifold" nearly coincide, with a few discrepancies owing to the fact that we have brazenly projected points in the augmented phase space onto a two-dimensional plane. In the full phase space, there are nontrivial differences between the z, z', E, and f coordinates of the "pseudo-manifold" points plotted in this figure and the domain of this FTLE field

The analyses above indicate that LCS in the three-body problem could play a guiding role for space mission design; LCSs often enclose regions of phase space whose composite trajectories exhibit desirable characteristics—in this instance, eventual entrance into the m_2 (Mercury) region. Using LCS to analyze the phase space structure for some mission design problems, particularly those for which certain mission constraints such as short flight times may be safely sacrificed, could offer a means of guiding the selection of initial guesses for trajectory optimization problems.

Finally, we note that the notion that BepiColombo's trajectory straddles an LCS of the spatial elliptic restricted three-body problem correlates well with previous studies of the BepiColombo mission. Campagnola and Lo (2007) have recognized that if one perturbs certain ER3BP quasiperiodic orbits about the Sun-Mercury L_1 in the direction of minimal stretching and examines the perturbed orbits' trajectories under the backward time flow (in a manner analogous to the traditional method of globalizing stable manifolds in the CR3BP), the resulting trajectories closely shadow the route of BepiColombo.

In light of these observations, it is worthwhile to compare the "pseudo-manifolds" described by Campagnola and Lo (2007) with the LCS already computed. Using the initial condition for a Sun-Mercury ER3BP L_1 Lissajous orbit studied by Campagnola and Lo (2007), we have computed the evolution of the orbit's state transition matrix over one revolution about L_1 and used the standard time-independent manifold globalization techniques (Parker and Chua 1989; Ross 2004) described in Sect. 1.2 to compute its stable

"pseudo-manifold"—the family of trajectories asymptotic to the quasiperiodic orbit. Figure 18 displays the projection of the $x = 0.99$ Poincaré cut of this "manifold" onto the $y - y'$ plane, superposed with the FTLE field of Fig. 15. Figure 18 should be interpreted with caution; by virtue of the nature of the standard manifold globalization method, examining the intersection of this "pseudo-manifold" with a plane in phase space that has codimension greater than one is infeasible. Thus, in the full phase space, there are nontrivial differences between the z, z', E, and f coordinates of the "pseudo-manifold" points plotted in the figure and the domain of the FTLE field, which is a two-dimensional ($x = \text{const.}$, $z = \text{const.}$, $z' = \text{const.}$, $E = \text{const.}$, $f = \text{const.}$) cross-section of the seven-dimensional (spatial) ER3BP augmented phase space. Nonetheless, Fig. 18 provides qualitative confirmation of the well-founded intuition that LCS are often the manifestations of phase space structures asymptotic to limit sets.

This notion is best understood by noting the relationship between LCS of time-dependent systems and invariant manifolds of their associated time-independent augmentations: For a non-autonomous system $\dot{\mathbf{q}} = \mathbf{f}(\mathbf{q}, t)$, we can identify LCS at any given instant as the constant-time cross sections of static invariant manifolds of the associated augmented system $\dot{\tilde{\mathbf{q}}} = \tilde{\mathbf{f}}(\tilde{\mathbf{q}})$, where $\tilde{\mathbf{q}} = (\mathbf{q}, t)$ and $\tilde{\mathbf{f}}(\tilde{\mathbf{q}}) = (\mathbf{f}(\mathbf{q}, t), 1)$. Consequently, we can expect tracers lying on repelling LCSs to approach invariant structures of the augmented system under the forward time flow. In our case, the limit sets of the augmented system correspond precisely to the quasiperiodic orbits, periodic orbits, and fixed points of the ER3BP.

4 Conclusions and further study

The results presented in this report demonstrate the existence of periodically pulsating LCS in the phase space of the elliptic restricted three-body problem which arise as the time-dependent analogues of stable and unstable manifolds of periodic orbits in the circular restricted three-body problem. The examination of cross sections of full-dimensional finite-time Lyapunov exponent fields proves to be an effective method of computing the intersections of these structures with surfaces of section in the ER3BP phase space, whose high dimension precludes the visualization of entire LCSs. As a concrete application, these results reveal the influence of orbital eccentricity on segments of the Interplanetary Transport Network associated with elliptically orbiting mass pairs.

Interestingly, LCS pulsation in the cases presented in Sects. 3.1–3.2 is characterized almost entirely by sinusoidal translation in E. An analytical explanation of this observation seems a worthy topic for further study. In addition, an investigation of the dual role that these structures play as both separatrices and as the invariant manifolds of quasiperiodic orbits deserves consideration; an interesting, albeit unsurprising, phenomenon is the observation that any tracer that lies on an ER3BP LCS eventually tends toward a quasiperiodic orbit.

This study has focused primarily on the planar elliptic restricted three-body problem in the case of small to moderate eccentricity; as such, an examination of LCS in the spatial ER3BP and a study of the effects of high eccentricity would make for a befitting complement to this investigation.

From a computational perspective, ridge extraction from three-dimensional FTLE fields presents a formidable challenge in a study such as this. The design of an automated ridge extraction algorithm for arbitrary-dimensional scalar fields would constitute an important advancement for the LCS community.

The use of a symplectic integrator might benefit this study, as the ER3BP is a Hamiltonian system. It is well-known that in the context of the numerical simulation of mechanical sys-

tems, structure-preserving integration algorithms such as variational integrators exhibit several desirable properties that traditional integration schemes generally do not, including exact momentum conservation, accurate energy behavior, and symplecticity (Marsden and West 2001). The extent to which such properties may influence the results of LCS computations for mechanical systems like the three-body problem is an issue yet to be studied in detail.

Finally, the computation of LCS in conjunction with the use of optimal control algorithms for space mission design constitutes an interesting prospect for further examination. LCS computation provides a general method for computing separatices in celestial systems that may or may not exhibit time dependence, offering a broader, less restrictive technique than the traditional manifold globalization approach that relies on the precalculation of limit sets. In turn, these separatrices may be used to guide the selection of initial guesses for some trajectory optimization problems, particularly those for which the benefits of fuel savings or recovery options outweigh the costs of lengthy transfer durations. The results reported in Sect. 3.4 illustrate this proposition, demonstrating the close relationship between LCS in the three-body problem and the Mercurial approach portion of ESA's BepiColombo mission.

Acknowledgements The authors would like to thank Michael Dellnitz, Wang-Sang Koon, Martin Lo, and Shane Ross for their helpful remarks, interest, and collaboration over the years.

References

Campagnola, S., Lo, M.: BepiColombo gravitational capture and the elliptic restricted three-body problem. In: 18th ICIAM07 6th International Congress on Industrial and Applied Mathematics, pp. 1–2. Zurich, Switzerland (2007)

Campagnola, S., Corral, C., Jehn, R., Yáñez, A.: Bepicolombo Mercury cornerstone mission analysis: inputs for the reassessment phase of the definition study. Tech. Rep. Mission Analysis Office Working Paper 452, ESA/ESOC (2003)

Campagnola, S., Jehn, R., Sanchez, N.: Bepicolombo Mercury cornerstone mission analysis: alternative transfer options and gravity field determination.Tech. Rep. Mission Analysis Office Working Paper 476, ESA/ESOC (2006)

Conley, C.: Low energy transit orbits in the restricted three-body problem. SIAM J. Appl. Math. **16**, 732–746 (1968)

Dellnitz, M., Junge, O., Koon, W.S., Lekien, F., Lo, M.W., Marsden, J.E., Padberg, K., Preis, R., Ross, S., Thiere, B.: Transport in dynamical astronomy and multibody problems. Int. J. Bifurc. Chaos **15**, 699–727 (2005)

Garcia, F., Gómez, G.: A note on weak stability boundaries. Celest. Mech. Dyn. Astron. **97**, 87–100 (2007)

Giorgini, J.D., Yeomans, D.K., Chamberlin, A.B., Chodas, P.W., Jacobson, R.A., Keesey, M.S., Lieske, J.H., Ostro, S.J., Standish, E.M., Wimberly, R.N.: JPL's on-line solar system data service. Bull. Am. Astron. Soc. **28**, 1158 (1996)

Goldstein, H., Poole, C., Safko, J.: Classical Mechanics. Addison Wesley, San Fransisco (2002)

Gómez, G., Koon, W.S., Lo, M., Marsden, J.E., Masdemont, J., Ross, S.D.: Invariant manifolds, the spatial three-body problem and space mission design. In: AAS/AIAA Astrodynamics Specialist Conference, pp. 1–20. Quebec City, Canada (2001)

Gómez, G., Koon, W.S., Lo, M., Marsden, J.E., Masdemont, J., Ross, S.D.: Connecting orbits and invariant manifolds in the spatial restricted three-body problem. Nonlinearity **17**, 1571–1606 (2004)

Haller, G.: Distinguished material surfaces and coherent structures in three-dimensional fluid flows. Physica D **149**, 248–277 (2001)

Jehn, R., Campagnola, S., Garcia, D., Kemble, S.: Low-thrust approach and gravitational capture at Mercury. In: 18th International Symposium on Space Flights Dynamics, pp. 1–6. Munich, Germany (2004)

Kemble, S.: Interplanetary Mission Analysis and Design. Springer, Berlin (2006)

Koon, W.S., Lo, M.W., Marsden, J.E., Ross, S.D.: The Genesis trajectory and heteroclinic connections. In: AAS/AIAA Astrodynamics Specialist Conference, pp. 99–451. Girdwood, Alaska (1999)

Koon, W.S., Lo, M., Marsden, J.E., Ross, S.D.: Heteroclinic connections between periodic orbits and resonance transitions in celestial mechanics. Chaos **10**, 427–469 (2000a)

Koon, W.S., Lo, M.W., Marsden, J.E., Ross, S.D.: Shoot the Moon. In: AAS/AIAA Astrodynamics Specialist Conference, pp. 1–8. Florida (2000b)
Koon, W.S., Lo, M.W., Marsden, J.E., Ross, S.D.: Dynamical systems, the three-body problem, and space mission design. In: Fiedler, B., Grger, K., Sprekels, J. (eds.) International Conference on Differential Equations, pp. 1167–1181.World Scientific, Berlin (2000c)
Koon, W.S., Lo, M., Marsden, J.E., Ross, S.D.: Resonance and capture of Jupiter comets. Celest. Mech. Dyn. Astron. **81**, 27–38 (2001)
Lekien, F., Shadden, S.C., Marsden, J.E.: Lagrangian coherent structures in n-dimensional systems. J. Math. Phys. **48**, 1–19 (2007)
Marsden, J.E., Ross, S.D.: New methods in celestial mechanics and mission design. Bull. Am. Math. Soc. **43**, 43–73 (2005)
Marsden, J.E., West, M.: Discrete mechanics and variational integrators. Acta Numer. **10**, 357–514 (2001)
Parker, T.S., Chua, L.O.: Practical Numerical Algorithms for Chaotic Systems. Springer-Verlag, New York (1989)
Perozzi, E., Di Salvo, A.: Novel spaceways for reaching the moon: an assessment for exploration. Celest. Mech. Dyn. Astron. **102**, 207–218 (2008)
Porter, M.A., Cvitanović, P.: Ground control to Niels Bohr: Exploring outer space with atomic physics. Not. Am. Math. Soc. **52**, 1020–1025 (2005)
Press, W.H., Teukolsky, S.A., Vetterling, W.T., Flannery, B.P.: Numerical Recipes in C: The Art of Scientific Computing. Cambridge University Press, New York (1992)
Ross, S.D.: Cylindrical manifolds and tube dynamics in the restricted three-body problem. Ph.D. thesis, California Institute of Technology, Pasadena, CA (2004)
Shadden, S.C., Lekien, F., Marsden, J.E.: Definition and properties of Lagrangian coherent structures from finite-time Lyapunov exponents in two-dimensional aperiodic flows. Physica D **212**, 271–304 (2005)
Szebehely, V.G.: Theory of Orbits: The Restricted Problem of Three Bodies. Academic Press, New York (1967)
Yeomans, D.K.: NASA jet propulsion laboratory: solar system dynamics. http://ssd.jpl.nasa.gov/ (2007)